IEEE Photonics Journal
An IEEE Photonics Society Publication

Open Access

Analysis on Beam Quality of Solid-State Tube MOPA System With Zigzag Beam Path

Volume 11, Number 2, April 2019

Boyu Tian
Zheqiang Zhong
Cong Huang
Xiaomin Zhang
Bin Zhang

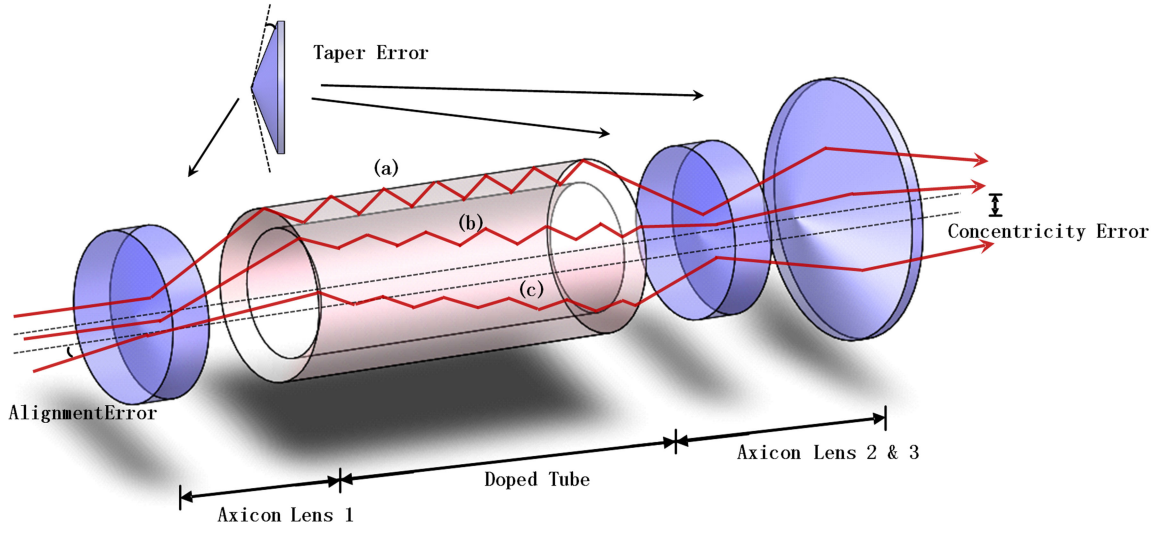

DOI: 10.1109/JPHOT.2019.2902396
1943-0655 © 2019 IEEE

IEEE photonics SOCIETY

IEEE

Analysis on Beam Quality of Solid-State Tube MOPA System With Zigzag Beam Path

Boyu Tian,[1] **Zheqiang Zhong**,[1] **Cong Huang**,[1] **Xiaomin Zhang**,[2] **and Bin Zhang**[1]

[1]School of Electronics and Information Engineering, Sichuan University, Chengdu 610064, China
[2]China Academy of Engineering Physics, Mianyang 621900, China

DOI:10.1109/JPHOT.2019.2902396

Manuscript received January 26, 2019; revised February 25, 2019; accepted February 26, 2019. Date of publication March 1, 2019; date of current version March 19, 2019. This work was supported by the Sichuan Science and Technology Program under Grant 2018JY0553. Corresponding author: Bin Zhang (e-mail: zhangbinff@sohu.com).

Abstract: All-solid-state tube lasers (ASSTLs) with zigzag beam path combine the attractive properties of rod, slab, and disk lasers. However, the analysis on the beam quality of tube lasers is rarely reported. In order to explore how and how seriously the static errors including fabricating and alignment errors degrade the beam quality of a tube laser, a theoretical model of a nonideal ASSTLs constructed in master oscillator power amplifier (MOPA) configuration has been built up by taking the static errors into consideration. On the basis, the influence of the fabricating and alignment errors on the static beam quality of the ASSTLs was analyzed in detail, and the annular aberration of the output beam was discussed as well. Simulation results indicate that the static beam quality of tube lasers strongly depends on the fabricating and alignment errors. These static errors would severely degrade the output beam quality of the ASSTLs and even result in coma and defocus aberrations. This work may provide valuable references for the design, processing, and applications of ASSTLs.

Index Terms: All-solid-state laser, zigzag path, beam quality, static error, aberration

1. Introduction

Thanks to the outstanding advantages of small size, light weight and high beam quality [1], all-solid-state lasers (ASSLs) have been broadly applied in the areas ranging from fabricating [2], information technology [3], laser spectroscopy [4], inertial confinement fusion [5], etc. However, ASSLs with high output power and good beam quality are highly desired for further progress owing to the unavoidable presence of the thermal lens effect and the thermal-stress induced birefringence in gain medium [6]–[13]. Fortunately, the slab laser with zigzag beam path was proposed to effectively diminish the wavefront distortion induced by thermal effects [14]. Zigzag propagation meets a relatively slight average temperature difference along the cross section of laser beams inside gain medium. Consequently, the wavefront distortion tends to reach a lower level, which can be easily compensated by an adaptive optical system [15].

However, there are some problems in slab lasers, examples of which are edge distortion and inefficient use of space. Fortunately, tube lasers provide a potential scheme to further bring up the output power without significantly degrading the beam quality of ASSLs [16]. A tube laser can

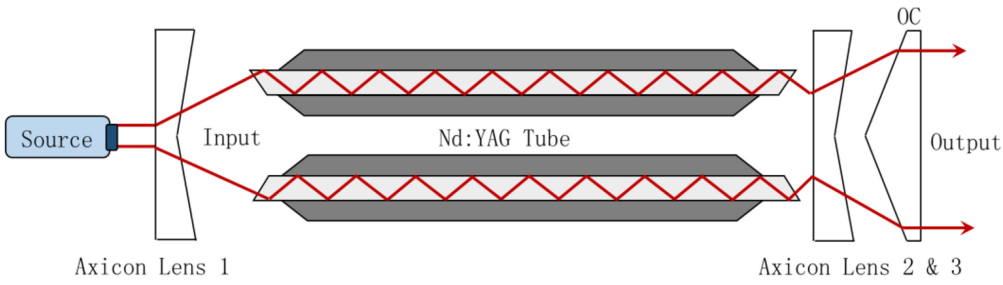

Fig. 1. Two-dimensional diagram of an Nd:YAG tube MOPA system. The circular beam passes through axicon lens 1 and transformed into annular beam, then the annular beam is amplified at the doped area and exists at axicon lens 3.

be considered as a rolled-up slab laser, thus it not only maintains the advantages of the slab configuration including small thermal distortion and light weight, but also exhibits its own unique advantages such as lack of edge distortion and more compact structure. Although there are some works on non-zigzag tube lasers [17], [18], to our knowledge, the study on the tube laser with zigzag path are rarely reported. Actually, the tubular configuration faces a new challenge to beam quality management compared to that in slab configuration, i.e., the parallel zigzag path would turn into a rotated zigzag path in a non-ideal tube arising from the fabricating and alignment errors. Furthermore, the non-ideal tube speeds up the degradation of the beam quality after each total internal reflection (TIR) on cylindrical surface of the tube.

In this paper, the static beam quality of ASSTLs degraded by the fabricating and alignment errors has been analyzed in detail. In order to reveal the evolution of the propagation path of laser beams in the tube medium, a theoretical model for the tube laser was proposed. The influence of the fabricating and alignment errors on the beam quality was analyzed in detail. Additionally, combining with annular Zernike aberrations analysis, the sensitivity factors leading to the degradation of the beam quality of tube lasers were determined.

2. Theoretical models

Figure 1 illustrates the two-dimensional section diagram of an Nd:YAG tube laser constructed in MOPA configuration. The light coupling system consists of axicon lens 1–3. The annular beam transformed from circular beam through axicon lens 1 and then obliquely incident into the doped tube medium. Thus, the zigzag beam is injected in the tube and transform to parallel annular beam by the axicon lenses 2 and 3. In this design, the pump scheme adopts inside-pump [16] or zigzag-pump along a spiral-shaped path [19].

Generally, the static errors of the tube laser amplifier mainly include the fabricating and alignment errors. The fabricating error is caused by the manufacturing defect and can be divided into the concentricity error and the taper error. Alignment error originates from the non-ideal aligning and installation. Actually, a Nd:YAG tube can be machined by drilling in a Nd:YAG rod. However, there is an inevitable problem that the fabricating error always exists in a processed tube. The structural parameters, examples of which are concentricity, taper, length and parallelism errors, cannot be controlled precisely due to the processing difficulty of high-hardened ceramic material [20], [21] like the Nd:YAG rod. Among these process errors or the fabricating errors, the length and parallel errors can be measured and then eliminated by the post-processing with the interferometric testing technique [22]. Consequently, only the concentricity and taper errors are considered as the main factors affecting the beam quality. Additionally, the alignment error of the system shown in Fig. 1 is also a key affecting factor because the beam quality is highly sensitive to the azimuth angle of light. The degradation of the beam quality caused by these errors is characterized by the beam path rotation and convergence (or divergence) in a non-ideal tube. Figure 2 shows the zigzag rotation paths in a non-ideal tube.

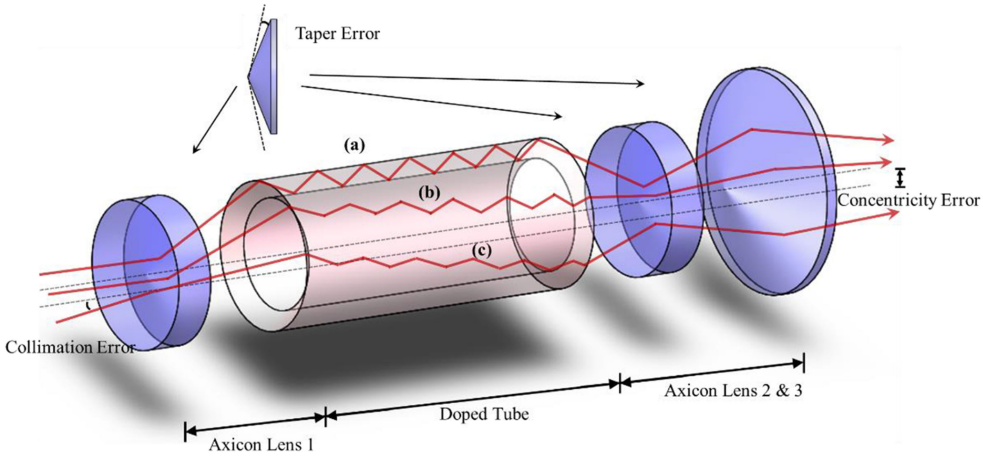

Fig. 2. Illustration of beam path rotation and convergence (or divergence) in non-ideal tube caused by (a) taper errors of a conical surfaces of axicon lens, (b) concentricity errors of a doped medium tube and (c) alignment error of input circular beam. Concentricity and alignment errors induced non-ideal propagation show a similar rotation tendency.

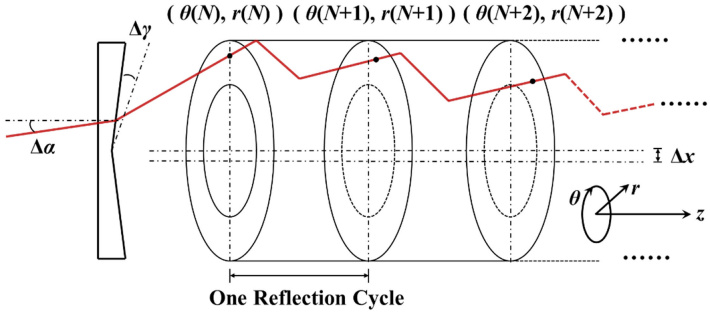

Fig. 3. Illustration of the rotation of rays after each TIR on outer and inner cylindrical surface.

For convenience for discussion but without loss of generality, we took a single-pass to analyze the influence of these errors on the beam quality in this paper. Although our analysis focuses on tube laser amplifiers, it is worth mentioning that this configuration can be applied in tube laser oscillator actually. According to the results of ray tracing, the rays tend to rotate in the tube due to the reflection point deviating from its ideal position and the distance between the ideal reflection point and the actual reflection point grows after each TIR. A theoretical model was built up to illustrate how the rays rotate in the tube, as shown in Fig. 3. We define $\theta\,(N)$ and $r\,(N)$ as the polar coordinates of the intersection of a zigzag ray and the cross section that perpendicular to the axis. Then, $\theta\,(N+1)$ and $r\,(N+1)$ are the polar coordinates of the intersection after two TIRs on the outer and inner cylindrical surfaces (one reflection cycle). When the errors are small, these cross sections are a series of equally spaced planes.

As shown in Fig. 3, the distance $|\Delta r\,(N)|$ between ($\theta\,(N)$, r (N)) and ($\theta\,(N+1)$, r ($N+1$)) is zero when the tube is ideal and the alignment error is eliminated. However, $|\Delta r\,(N)|$ will increase rapidly with the growth of N in a non-ideal tube when fabricating and alignment errors exist.

In order to derive an analytic expression of coordinates, we made some approximations in the derivation and followed the method of geometrical optics. As shown in Fig. 4(a), the rays are obliquely incident to the tube with an angle θ_c. h is wall thickness of the tube, $\Delta\gamma$ is accumulated taper error of the system. R_o and R_i are the outer and the inner radius of the tube, respectively. The maximum cycle of the rays in the tube is $N_{max} = (K-1)/2$, where K is reflection number. Due to the

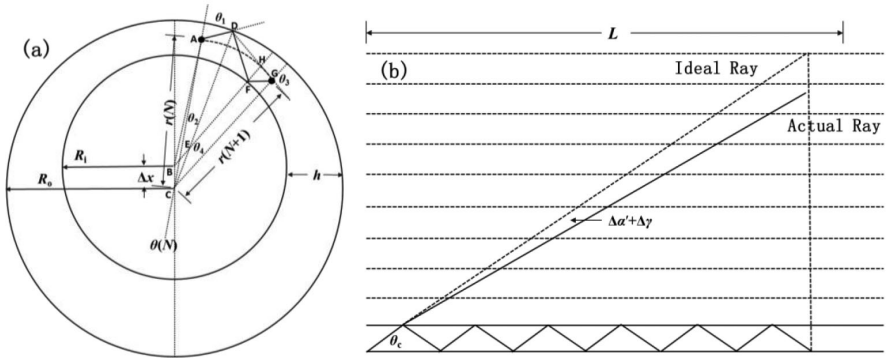

Fig. 4. Ray tracing of non-ideal rays in the tube with fabricating and alignment errors.

fabricating and alignment error, θ_1 is the summation of angle BAC and the transverse component of alignment error $\delta\theta$ where

$$\delta_\theta = \arccos\left[\frac{\vec{r}\,\vec{r_a}}{|\vec{r}|\,|\vec{r_a}|}\right] \tag{1}$$

Assuming that δ_θ is constant in propagation and using law of sine in triangle ABC, we obtain

$$\frac{R_i}{\sin\theta(N)} = \frac{\Delta x}{\sin\theta_1 - \delta_\theta} \tag{2}$$

Then, θ_1 can be written as

$$\theta_1 = \arcsin\left(\frac{\Delta x}{R_i}\sin\theta(N)\right) + \delta_\theta \tag{3}$$

Usually, the transverse component of alignment error and fabricating error are small, indicating that θ_1 is close to zero. Thus

$$l_{AD} \approx \frac{R_o - r(N)}{\cos\theta_1} \tag{4}$$

Similarly to above derivation, by the use of sine in triangle ACD, θ_2 is given by

$$\theta_2 = \arcsin\left(\frac{R_o - r(N)}{R_o}\frac{\sin\theta_1}{\cos\theta_1}\right) = \arcsin\left(\frac{R_o - r(N)}{R_o}\tan\theta_1\right) \tag{5}$$

Generally, the tube needs to be processed into a wide tube with thin wall to achieve a good heat dissipation performance and large effective gain volume. In other words, the thickness of wall h is far less than the inner radius R_i. Thus, angle CDF is close to angle CDG. By using law of sine in triangle CDG, θ_3 can be written as

$$\theta_3 = \arcsin\left(\frac{R_o}{r(N)}\sin(\theta_1 - \theta_2)\right) + \frac{\pi}{2} \tag{6}$$

According to the geometrical relation, we can get

$$\begin{aligned}\theta(N+1) &= \theta(N) + \theta_2 - \theta_3 - \angle CDG + \frac{\pi}{2} = \theta(N) - \arcsin\left(\frac{\Delta x}{R_i}\sin\theta(N)\right) + \delta_\theta + 2\arcsin \\ &\times\left(\frac{R_0 - r(N)}{R_o}\tan\left(\arcsin\left(\frac{\Delta x}{R_i}\sin\theta(N)\right) + \delta_\theta\right)\right) - \arcsin\left\{\frac{R_o}{r(N)}\sin\left[\arcsin\left(\frac{\Delta x}{R_i}\sin\theta(N)\right)\right.\right. \\ &\left.\left. + \delta_\theta - \arcsin\left(\frac{R_0 - r(N)}{R_o}\tan\left(\arcsin\left(\frac{\Delta x}{R_i}\sin\theta(N)\right) + \delta_\theta\right)\right)\right]\right\}\end{aligned} \tag{7}$$

and its simplified form

$$\theta(N)|_{N>1} \approx \theta(1) + 2\sum_{k=1}^{N-1}\left[\frac{r(k)}{R_o} - 1\right]\left[\frac{\Delta x}{R_i}\sin\theta(k) + \delta_\theta\right] \tag{8}$$

Followed by the derivation of $r(N+1)$, which is much easier. As shown in Fig. 4(b), the zigzag path in one-layer medium is equal to the straight path in multi-layer medium. When take alignment error $\Delta\alpha$ and taper error $\Delta\gamma$ into consideration, $r(N+1)$ can be derived as

$$r(N+1) = r(N) + \frac{L}{N_{\max}}\left[\tan\theta_c - \tan\left(\theta_c - \Delta\alpha' - \Delta\gamma\right)\right] \tag{9}$$

whose simplified form is

$$r(N)|_{N>1} \approx r(1) + \frac{(N-1)(\Delta\alpha' + \Delta\gamma)L}{N_{\max}\cos^2\theta_c} \tag{10}$$

where $\Delta\alpha'$ is the longitudinal component of $\Delta\alpha$.

According to the derivation above, we got the recursion formulas of $\theta(N+1)$ and $r(N+1)$. It is worth pointing out that the derivation only holds true under the conditions that all the errors are small enough and h is far less than R_i. Further, the offset rate of ray path is defined as

$$a(N)|_{N>1} = \frac{|\Delta r(N+1)| - |\Delta r(N)|}{|\Delta r(N)| - |\Delta r(N-1)|} \tag{11}$$

where

$$\left|\Delta\vec{r}(N)\right| = \sqrt{[r(N)\cos\theta(N) - r(N-1)\cos\theta(N-1)]^2 + [r(N)\sin\theta(N) - r(N-1)\sin\theta(N-1)]^2} \tag{12}$$

In order to obtain the simplified form of Eq. (12), we use the approximations of triangle. Then, Eq. (12) can be written as

$$\left|\Delta\vec{r}(N)\right| = \sqrt{\Delta r^2 + \Delta\theta^2 r^2(N)} = \sqrt{\frac{(\Delta\alpha' + \Delta\gamma)^2 L^2}{N_{\max}^2\cos^4\theta_c} + 4r^2(N)\left[\frac{r(N-1)}{R_o} - 1\right]^2\left[\frac{\Delta x}{R_i}\sin\theta(N-1) + \delta_\theta\right]^2} \tag{13}$$

The offset rate $a(N)$ describes how a ray path evolves along the azimuthal direction in a non-ideal tube. $a(N) > 1$ implies that the errors enhance the ray rotation after each TIR, while $a(N) < 1$ means that the rotation is slowly growing. If $a(N)$ equals 1, the ray rotates at a constant rate.

In this paper, the beam quality in the far field is diagnosed by the power in bucket (PIB), factor β and annular Zernike polynomials expansion. PIB is a key parameter for describing the proportion of energy in bucket to the total energy, and can be expressed as [23]

$$\mathrm{PIB} = \frac{\int_{\mathrm{Bucket}} I(x,y)\,dxdy}{\int_{\mathrm{AllArea}} I(x,y)\,dxdy} \tag{14}$$

where $I(x, y)$ is light intensity distribution function, and the "Bucket" means target area in bucket.

The focusing ability of laser beams is characterized by β factor [24]

$$\beta = \frac{r}{r_{\mathrm{LD}}} \tag{15}$$

For PIB = 86.5%, where r_{LD} is radius of ideal focal spot in diffraction limit, and r labels radius of bucket of real focal spot. Usually, the focal spot is asymmetric under non-ideal propagation conditions. Hence, the center of bucket can be defined as the barycenter of focal spot $\bar{x}$ and $\bar{y}$, i.e.,

$$\bar{x} = \frac{\int_{\mathrm{AllArea}} xI(x,y)dxdy}{\int_{\mathrm{AllArea}} I(x,y)dxdy} \tag{16}$$

$$\bar{y} = \frac{\int_{\mathrm{AllArea}} yI(x,y)dxdy}{\int_{\mathrm{AllArea}} I(x,y)dxdy} \tag{17}$$

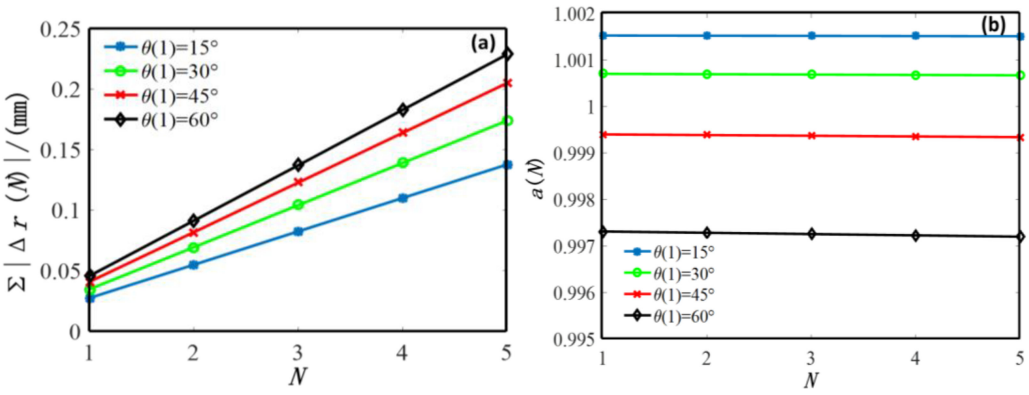

Fig. 5. Variation of the (a) total offset $\Sigma|\Delta r(N)|$; (b) offset rate $a(N)$ with different total reflection cycle N.

3. Simulation Results and Analysis

A theoretical model has been built in section 2 based on which the evolution of the ray path was analyzed in section 3.1. The impact of fabricating and alignment errors on the beam quality of tube laser amplifiers was studied in section 3.2. The impact of tubular configuration on the polarization state was discussed in section 3.3 as well as the sensitive factors that degrade the beam quality. Finally, the requirements of the fabricating accuracy and the alignment precision were proposed to improve the static beam quality of tube laser amplifiers.

3.1 Analysis of the Non-Ideal Zigzag Path

Based on the theoretical model, the evolution of the zigzag path in a non-ideal tube was analyzed. The incident beam is radial polarized. The laser wavelength is 1064 nm [25]. The refractive index of Nd:YAG is 1.83 [26].The parameters of the non-ideal tube are: The inner and outer radius of tube R_i and R_o are 15 mm and 20 mm, respectively. The length of the doped tube L is 90.58 mm, and critical angle of reflection θ_c in tube is 33.69°. The concentricity error is $\Delta x = 20$ μm (along the direction of $\theta(N) = 0$), the accumulated taper error is $\Delta\gamma = 50$ μrad and the alignment error is $\Delta\alpha = 3$ mrad. When the reflection cycle N is 5, some simulation results are presented in Fig. 4. A ray with different incident azimuthal angle $\theta(1)$ incidents at the same radius $r(1) = 17.5$ mm.

As illustrated in Fig. 5(a), the rays incident with different azimuthal angles exhibit different offset rates and position offsets. However, the total offset shows an increasing trend no matter where the incident rays are. As shown in Fig. 5(b), the critical azimuthal angle σ_c is 42° according to simulation results. That is to say, when $\theta(1)$ is smaller than the critical azimuthal angle σ_c, the offset rate is larger than 1 which means the rotation of the rays is intensified, and vice versa. The angle-varying $a(N)$ causes the nonuniformity of offset that results in the non-uniform rotation of rays, and unfortunately, the non-uniform rotation of the rays results in the wavefront distortion.

Besides static errors, the offset of rays is also sensitive to the total reflection cycle N, as shown in Fig. 5(a). It can be seen that the total offset $\Sigma|\Delta r(N)|$ nearly linearly increases with the increasing of N. Based on Eq. (13), we make an further approximation

$$\left[\frac{r(N-1)}{R_o} - 1\right]^2\Bigg|_{h \ll R_i} \approx 0 \tag{18}$$

and an simplifed form of total offset can be derived, i.e.,

$$\sum\left|\Delta\vec{r}(N)\right| \approx \frac{NL(\Delta\alpha' + \Delta\gamma)}{N_{max}\cos^2\theta_c} \tag{19}$$

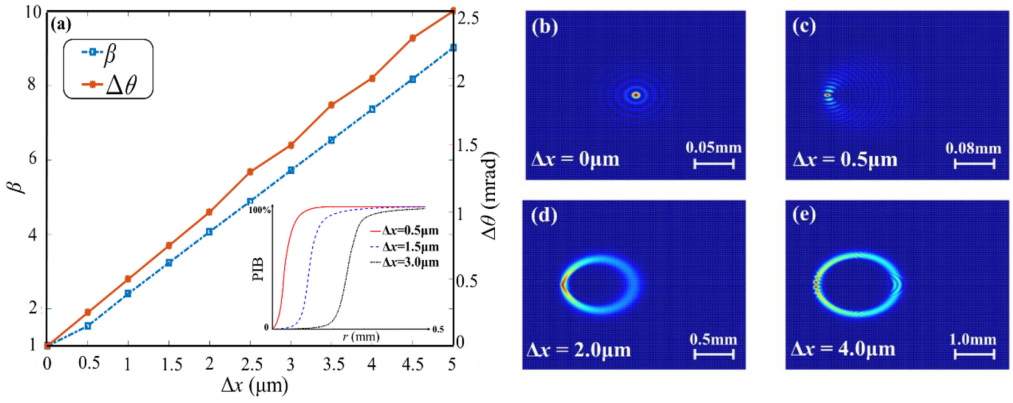

Fig. 6. (a) Variation of β factor and tilted angle $\Delta\theta$ of output beam for different concentricity error Δx; (b)–(e) Intensity distributions for different Δx of 0 μm, 0.5 μm, 2.0 μm and 4.0 μm.

Eq. (19) gives an approximate analytical expression of total offset, which explains the nearly linearly relationship between the total offset and reflection cycle, as shown in Fig. 5(a). As a result, the total offset will reach an unacceptable scale ($\sim$millimeter-scale) if static errors were not controlled well for the case of the tube with relatively longer length.

3.2 Fabricating and Alignment Errors

Now, we analyze the influence of the concentricity error and the taper error on the beam quality, respectively. In this part, the simulations are based on the Advanced System Analysis Program (ASAP) software, which provides wave optics method to simulate the phase evolution for different skewed rays and computes the intensity distribution of beam. The width of annular light is 5 mm, and output annular beam is focused by a lens with focal length $f = 400$ mm. The output beam is an annular beam with an outer radius of 26.5 mm and an inner radius of 21.5 mm, whose obscure ratio ε is 0.811. The reflection number K is 11.

3.2.1 Beam-Quality Degradation Induced by Fabricating Errors: As mentioned above, a potential way to process a YAG tube is punching on a YAG rod. However, this process would mainly lead to concentricity and taper errors. Figure 6(a) shows the variation of β factor and the tilted angle $\Delta\theta$ of the output beam with the increasing of the concentricity error, and the corresponding variation of the focal spots with different concentricity errors are given in Figs. 6(b)–(e).

Figure 6(a) illustrates the beam quality of output beam degrades rapidly and almost linearly with the increasing of the concentricity error Δx. The annular beam is focused well and exhibits a high beam quality ($\beta < 1.5$) when the concentricity errors Δx is less than 0.5 μm, as shown in Fig. 6(b). In addition, an obvious deformation of focal spot pattern appears when Δx exceeds 0.5μm, as shown in Figs. 6(c)–(e). Figure 6(d) implies that the deformation of the focal spot becomes severe for $\Delta x = 2$ μm. If Δx is higher than 4 μm, the focal spot of annular beam becomes a donut shape with $\beta > 7$, as shown in Fig. 6(a) and (e). Meanwhile, the inset of Fig. 6(a) shows the encircled energy drops with the increasing of Δx from 0.5 to 3.0 μm. Besides, the tilted angle $\Delta\theta$ of the wavefront of the output annular beam increases with the increasing of Δx, and the wavefront of the output annular beam is tilted, as illustrated in Fig. 6(a). In particular, the rotation of rays in same direction at the output end of the tube gives rise to the tilt of the wavefront. Therefore, the tilted angle $\Delta\theta$ induced by the concentricity error can even reach several milliradians for relatively large value of Δx.

Another important factor degrading the beam-quality is the taper error $\Delta\gamma$ contributed by the conical surface, and the degradation of the beam quality manifests as the convergence or divergence of the focal spot. For simplicity but without loss of generality, the tube laser with the taper error is equivalent to an ideal system with an extra axicon lens and an accumulated taper angle of γ' at its output end, as illustrated in Tab. 1.

TABLE 1
Taper Error Induced Defocus and Degradation of Beam Quality

$\Delta\gamma$ (μrad)	10	20	30	40	50
β	1.2	1.4	1.6	1.8	2.0
Δf (mm)	0.7	1.4	2.2	2.9	3.6
γ' (°)	179.997	179.994	179.992	179.989	179.986

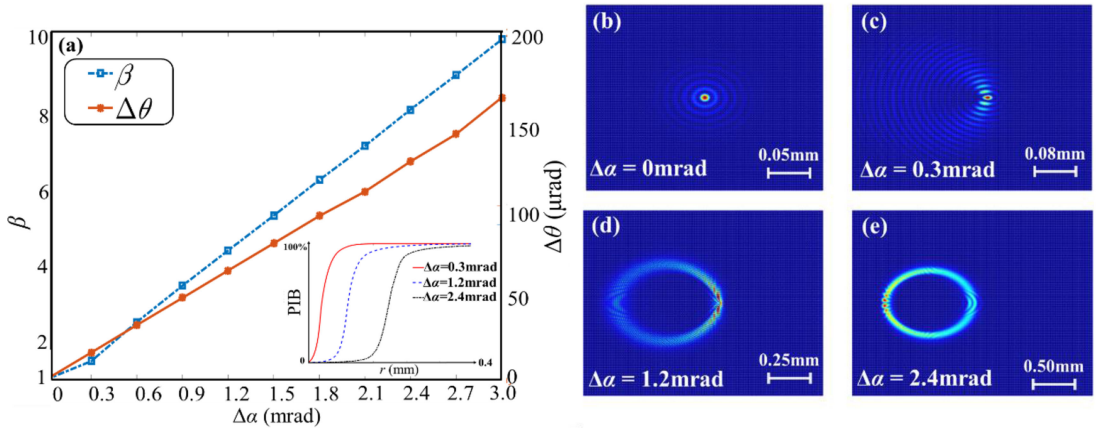

Fig. 7. (a) Variation of β factor and the tilted angle $\Delta\theta$ of output light with the alignment error $\Delta\alpha$; (b)–(e) Intensity distribution for different $\Delta\alpha$ of 0 mrad, 0.3 mrad, 1.2 mrad and 2.4 mrad.

It can be concluded from Tab. 1 that the equivalent axicon is a relatively flat cone, and the size of the focal spot is slightly larger than ideal diffraction limit (DL) when the accumulated taper error $\Delta\gamma$ *is* sub-milliradian scale. Correspondingly, the degradation of the beam quality is mainly induced by Δx, because $\Delta\gamma$ at the order of milliradian-scale is easier to be controlled than Δx at a micron-scale level. Therefore, concentricity accuracy at submicron-scale level and cone accuracy at microradians-scale are essential in the control of the fabricating process to improve the performance of tube lasers.

3.2.2 Beam Quality Degradation Induced by Alignment Error: According to the results of ray tracing, the alignment error also results in the rotation of rays in the tube, and further brings about the degradation of the beam quality.

As shown in Fig. 7, the degradation of the beam quality induced by the alignment error is similar to that by the concentricity error. The focal spot will also evolve into a donut shape when $\Delta\alpha$ increases to a certain scale. However, the tilt angle $\Delta\theta$ induced by the alignment error is one order of magnitude less than that by the concentricity error for a given β factor, meaning that the tilt angle $\Delta\theta$ is lower sensitive to the alignment error than to the concentricity error. Thus, another key factor for achieving a good beam quality is to precisely control the alignment error at the sub-milliradian scale.

3.3 Analysis of the Polarization State and Wavefront Evolution

3.3.1 The Polarization State of Annular Light: In the analysis above, we assumed that the polarization state of incident beam was radial polarization. The impact of tubular configuration on the evolution of polarization state was not considered. In the following simulation, we assumed that the incident beam is linear polarized light and the optical coatings do not have the selectivity to polarization state. Due to the Goos-Hanchen shift, the s wave and the p wave generate different phase mutations after TIR. The polarized light E can be decomposed into E_s and E_P, and the field

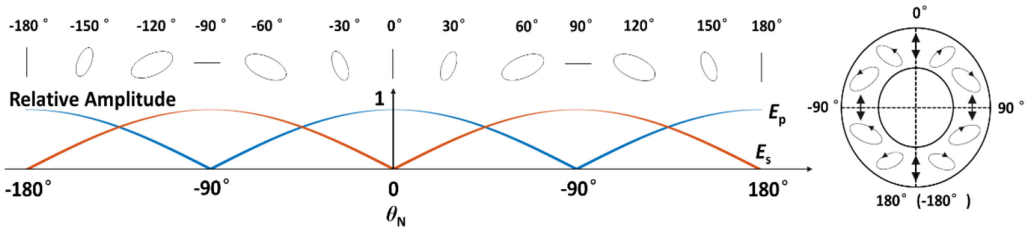

Fig. 8. The polarization state distribution of output annular light.

for the reflected light can be derived according to the Fresnel's Formula, i.e.,

$$E_s^r = \frac{\cos\ \theta_1 - i\sqrt{\sin^2\ \theta_1 - n^2}}{\cos\ \theta_1 + i\sqrt{\sin^2\ \theta_1 - n^2}} E_s = |E_s| \exp\left(i\varphi_s\right) \tag{20}$$

$$E_p^r = \frac{n^2 \cos\ \theta_1 - i\sqrt{\sin^2\ \theta_1 - n^2}}{n^2 \cos\ \theta_1 + i\sqrt{\sin^2\ \theta_1 - n^2}} E_p = \left|E_p\right| \exp\left(i\varphi_p\right) \tag{21}$$

where n is n_{air}/ n_{YAG} which stands for relative refractive index. Actually, φ_s and φ_p are usually unequal, and can be expressed as

$$\varphi_s = \sum_N \arctan \frac{2\cos\ \theta_1 \sqrt{\sin^2\ \theta_1 - n^2}}{\sin^2\ \theta_1 - n^2 - \cos^2\ \theta_1} \tag{22}$$

$$\varphi_p = \sum_N \arctan \frac{2n^2 \cos\ \theta_1 \sqrt{\sin^2\ \theta_1 - n^2}}{\sin^2\ \theta_1 - n^2 - n^4 \cos^2\ \theta_1} \tag{23}$$

Fig. 8 shows the polarization state distribution of output annular light and it reveals that the linear polarized light is transformed to the elliptically polarized light after passing through the tube. On account of the variation of the ratio of E_p to E_s, the direction of long axis of the ellipse changes with the incident azimuthal angle. Particularly, only the polarization state of rays whose $\theta(N)$ are 0°, 90°, −90° and 180° remains unchanged. Thus, in order to achieve a good beam quality, the polarization state of the incident beam must be centrosymmetric such as radial polarization.

3.3.2 The Wavefront Evolution and Aberration Analysis: According to the preliminary analysis, the dispersion of focal spot is sensitive to the alignment error, and the tilt of output wavefront is sensitive to fabricating error. The impact of taper error on beam quality is relatively slight. In order to further illustrate the degradation characteristics of the beam quality, the aberrations of the beam were analyzed based on the annular Zernike polynomials decomposition theory of wavefront aberration [27]. The annular Zernike polynomials form a complete orthogonal and rotational-invariance set for the interior of a unit circle with central obscuration which can represent the aberrations of a system with annular pupil. When decomposing the wavefront by the least square fitting method, the wavefront is treated as a multiplicative summation of the annular Zernike polynomials and the Zernike coefficients. Due to the errors of the tube, the wavefront of the output beam is not an ideal ring. Although some high-order simulation errors will occur when fitting the non-ideal annular wavefront with the Zernike polynomials, this theory still shows high accuracy in aberration analysis. Each annular aberration has its own corresponding annular Zernike coefficient. The following analysis focuses on the fabricating and alignment errors and only one kind of errors was considered during each simulation. The aberrations of the output beam are given in Fig. 9.

As shown in Fig. 9, no matter what kind of error was considered, the main aberrations are tilt, defocus and coma which correspond to order n = 2, 4 and 7, respectively. The wavefront distortion caused by the fabricating and alignment errors exhibit almost the same main aberration forms. Similarly, the proportion of tilt aberration is much larger than other aberrations. Furthermore, the wavefront distortion along the angular direction is also obvious and brings about a significant coma

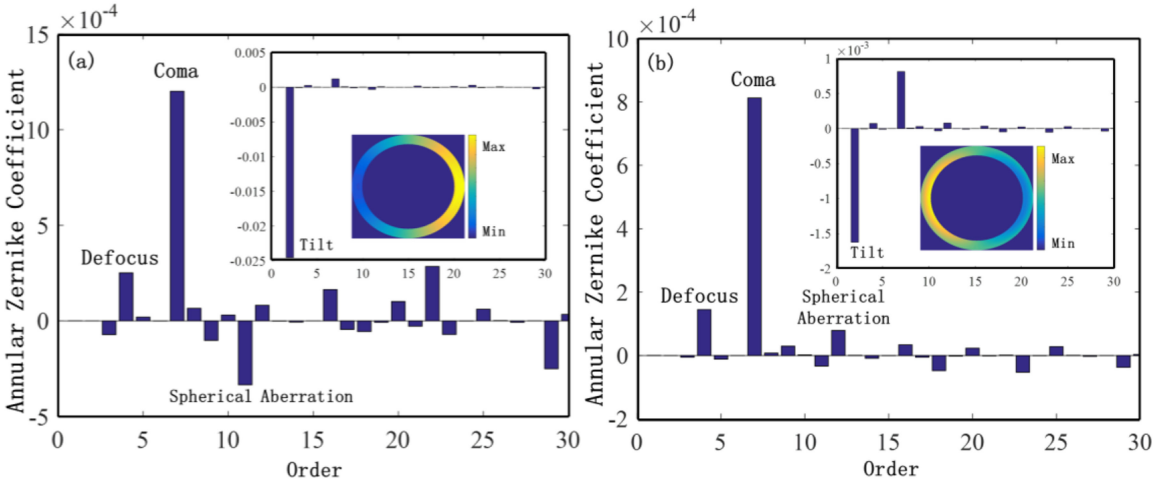

Fig. 9. (a) Concentricity error ($\Delta x = 2.5\ \mu$m) and (b) alignment error ($\Delta\alpha = 2.5$ mrad) induced wavefront distortion and annular Zernike coefficients.

aberration. That is the reason why the focal spot appears to disperse when the fabricating or alignment errors reaches a certain degree as shown in Figs. 6 and 7. All these characteristics demonstrate that the non-uniform rotation of the rays leads to the wavefront distortion. To show a more dynamic range for higher order coefficients, we ignored the tilt aberration, and this treatment is rational because the tilt aberration usually depends on the viewing angle. It can be seen that the details of aberrations induced by concentricity error and alignment error are slightly different. Both aberrations, except for main aberrations, include astigmatism, high-order coma, spherical and high-order astigmatism aberrations corresponding to n = 5, 9, 11 and 12, respectively. However, the proportion of aberrations is different.

It is worth noting that the proportion of the main aberration caused by the fabricating error and the alignment error is different. Specifically, for the wavefront distortion caused by the fabricating error, the tilt is the main aberration, whereas the defocus and coma aberrations are relatively small. However, for the wavefront distortion caused by the alignment error, the defocus and coma aberrations have a higher proportion than that caused by the concentricity error. Based on the above analysis, the tilt aberration is more sensitive to the fabrication error whereas the coma aberration is more sensitive to the alignment error.

It can be concluded from above analysis that the tube laser presents a new challenge to beam quality control. The static errors degrade the static beam quality seriously, which are usually not the main problem in other lasers (such as rod, slab and disk lasers). Under the active condition, the refractive index change is sensitive to the temperature and the active wavefront distortion will get worse with the increasing of pumping levels. Consequently, the pump-induced refractive index change will further degrade the beam quality [28] and the peak-to–valley of the active wavefront distortion can reach or even exceed the level of λ [29]. Fortunately, the zigzag optical path in tube lasers is benefit for compensating the effect of the pump-induced refractive index change on the beam quality.

4. Conclusions

The tube laser is a potential approach to generate laser beams with high beam quality. In order to analyze the influence of the key factors on the static beam quality, the theoretical model of a non-ideal tube laser amplifier with zigzag path has been built up. The spiral path of actual zigzag ray was analyzed, as well as the impact of the fabricating and alignment errors on the beam quality. Further, the evolution of polarization state was discussed and the annular aberration analysis was

carried out to illustrate the aberration component of the non-ideal wavefront. The results indicate that the fabricating error and alignment error are two main factors that contribute to the degradation of the beam quality of tube lasers. The tilt, defocus and coma aberrations of the wavefront are sensitive to the concentricity, taper and alignment errors, respectively. To ensure the performance of tube lasers, the submicron-scale level of concentricity accuracy, microradians-scale of cone accuracy and sub-milliradian level of alignment accuracy are required in fabricating and adjustment of tube laser.

References

[1] T. Y. Fan and R. L. Byer, "Diode laser-pumped solid-state lasers," *Science*, vol. 239, no. 4841, pp. 742–747, Feb. 1988.
[2] K Venkatesan, "The study on force, surface integrity, tool life and chip on laser assisted machining of Inconel 718 using Nd:YAG laser source," *J. Adv. Res.*, vol. 8, no. 4, pp. 407–423, Jul. 2017.
[3] H Li and X Sang, "SNR and transmission error rate for remote laser communication system in real atmosphere channel," *Sens. Actuator A—Phys.*, vol. 258, no. 2017, pp. 156–162, May 2017.
[4] R. Pohl *et al.*, "Laser spectroscopy of muonic deuterium," *Science*, vol. 353, no. 6300, pp. 669–673, Aug. 2016.
[5] E. I. Moses, "Ignition on the national ignition facility," *Opt. Eng.*, vol. 43, no. 12, pp. 21–51, May 2002.
[6] W. Xie *et al.*, "Influence of the thermal effect on the TEM_00 mode output power of a laser-diode side-pumped solid-state laser," *Appl. Opt.*, vol. 39, no. 30, pp. 5482–5487, Oct. 2000.
[7] L. M Osterink and J. D. Foster, "Thermal effects and transverse mode control in a Nd:YAG laSER," *Appl. Phys. Lett.*, vol. 12, no. 4, pp. 128–131, Feb. 1968.
[8] X. Yan *et al.*, "Numerical modeling of the thermal lensing effect in a grazing-incidence laser," *Opt. Commun.*, vol. 282, no. 9, pp. 1851–1857, May 2009.
[9] I. Shoji *et al.*, "Thermal-birefringence-induced depolarization in Nd:YAG ceramics," *Opt. Lett.*, vol. 27, no. 4, pp. 234–236, Feb. 2002.
[10] M. Li *et al.*, "A 7.08-kW YAG/Nd:YAG/YAG composite ceramic slab laser with dual concentration doping," *IEEE Photon. J.*, vol. 9, no. 4, Jun. 2017, Art. no. 1504010.
[11] J. S. Shin *et al.*, "Design of pump beam delivering optical system and doped YAG length to minimize the wavefront distortion in a high-power Nd:YAG zigzag slab laser," *Opt. Eng.*, vol. 56, no. 1, pp. 016109–1–016109–6, Jan. 2017.
[12] J. S. Shin *et al.*, "Wavefront improvement in an end-pumped high-power Nd:YAG zigzag slab laser," *Opt. Express*, vol. 25, no. 16, pp. 19309–19319, Aug. 2017.
[13] Y. Y. Lin *et al.*, "High-pulse-energy topological insulator Bi2Te3-based passive Q-switched solid-state laser," *IEEE Photon. J.*, vol. 8, no. 4, Aug. 2016, Art. no. 1502710.
[14] J. S. Shin *et al.*, "Simulation of the wavefront distortion and beam quality for a high-power zigzag slab laser," *Opt. Commun.*, vol. 380, no. 2016, pp. 446–451, Dec. 2016.
[15] P. Yang *et al.*, "Enhancement of the beam quality of non-uniform output slab laser amplifier with a 39-actuator rectangular piezoelectric deformable mirror," *Opt. Express*, vol. 18, no. 7, pp. 7121–7130, Mar. 2010.
[16] U. Wittrock, B. Eppich, and H. Weber, "Inside-pumped Nd:YAG tube laser," *Opt. Lett.*, vol. 16, no. 14, pp. 1092–1094, Jul. 1991.
[17] R. A. Chodzko *et al.*, "Annular (HSURIA) resonators: Some experimental studies including polarization effects," *Appl. Opt.*, vol. 19, no. 5, pp. 778–789, Mar. 1980.
[18] U. Wittrock, B. Eppich, and H. Weber, "Beam quality of the 1-kW inside-pumped Nd:YAG tube laser," in *Proc. Conf. Lasers Electro-Opt.*, 1992.
[19] M. Savich, "High power tube solid-state laser with zigzag propagation of pump and laser beam," in *Proc. SPIE —Int. Soc. Opt. Eng.*, 2015, pp. 934216–1–934216–9.
[20] J. Cheng *et al.*, "Study on grinding force modelling and ductile regime propelling technology in micro drill-grinding of hard-brittle materials," *J. Mater. Process. Technol.*, vol. 223, no. 2015, pp. 150–163, Sep. 2015.
[21] H. H. Su *et al.*, "Study on machining of hard-brittle materials with thin-walled monolayer brazed diamond core drill," *Mater. Sci. Forum*, vol. 223, no. 2015, pp. 150–163, Apr. 2015.
[22] H. Liu, Z. Lu, and F. Li, "Using diffractive optical element and Zygo interferometer to test large-aperture convex surface," *Opt. Laser Technol.*, vol. 37, no. 8, pp. 642–646, Nov. 2005.
[23] X. Kang and B. Lü, "Vectorial nonparaxial flattened gaussian beams and their beam quality in terms of the power in the bucket," *Opt. Commun.*, vol. 262, no. 1, pp. 1–7, Jun. 2006.
[24] V. N. Mahajan, "Zernike annular polynomials for imaging systems with annular pupils," *J. Opt. Soc. Amer.*, vol. 71, no. 1, pp. 75–85, Jan. 1981.
[25] L. Chen *et al.*, "Continuous-wave tri-wavelength operation at 1064, 1319 and 1338 nm of LD end-pumped Nd:YAG ceramic laser," *Opt. Express*, vol. 18, no. 21, pp. 22167–22173, Oct. 2010.
[26] O. L. Antipov, O. N. Eremeykin, A. P. Savikin, V. A. Vorob'ev, D. V. Bredikhin, and M. S. Kuznetsov, "Electronic changes of refractive index in intensively pumped Nd:YAG laser crystals," *IEEE J. Quantum Electron.*, vol. 39, no. 7, pp. 910–918, Jul. 2003.
[27] V. N. Mahajan, "Zernike annular polynomials and optical aberrations of systems with annular pupils," *Appl. Opt.*, vol. 33, no. 34, pp. 8125–8127, Dec. 1994.
[28] C. Pfistner *et al.*, "Thermal beam distortions in end-pumped Nd:YAG, Nd:GSGG, and Nd:YLF rods," *IEEE J. Quantum Electron.*, vol. 30, no. 7, pp. 1605–1615, Jul. 1994.
[29] X. Zhang, X. Zhang, and A. Xiang, "Analysis of thermal effect and beam wavefront properties for LD-pumped Q-switch Nd:YAG laser," *Opt. Laser Technol.*, vol. 49, pp. 268–273, Jul. 2013.